DHA-containing phospholipids control membrane fusion and transcellular tunnel dynamics

Meng-Chen Tsai, Lucile Fleuriot, Sébastien Janel, David Gonzalez-Rodriguez, Camille Morel, Amel Mettouchi, Delphine Debayle, Stéphane Dallongeville, Jean-Christophe Olivo-Marin, Bruno Antonny, et al.

▶ **To cite this version:**

Meng-Chen Tsai, Lucile Fleuriot, Sébastien Janel, David Gonzalez-Rodriguez, Camille Morel, et al.. DHA-containing phospholipids control membrane fusion and transcellular tunnel dynamics. Journal of Cell Science, 2022, 135 (5), pp.jcs259119. 10.1242/jcs.259119 . pasteur-03744949

HAL Id: pasteur-03744949
https://pasteur.hal.science/pasteur-03744949v1

Submitted on 3 Aug 2022

HAL is a multi-disciplinary open access archive for the deposit and dissemination of scientific research documents, whether they are published or not. The documents may come from teaching and research institutions in France or abroad, or from public or private research centers.

L'archive ouverte pluridisciplinaire **HAL**, est destinée au dépôt et à la diffusion de documents scientifiques de niveau recherche, publiés ou non, émanant des établissements d'enseignement et de recherche français ou étrangers, des laboratoires publics ou privés.

Copyright

© 2022. Published by The Company of Biologists Ltd | Journal of Cell Science (2022) 135, jcs259119. doi:10.1242/jcs.259119

RESEARCH ARTICLE

SPECIAL ISSUE: CELL BIOLOGY OF LIPIDS

DHA-containing phospholipids control membrane fusion and transcellular tunnel dynamics

Meng-Chen Tsai[1,2], Lucile Fleuriot[1], Sébastien Janel[3], David Gonzalez-Rodriguez[4], Camille Morel[2], Amel Mettouchi[2], Delphine Debayle[1], Stéphane Dallongeville[5], Jean-Christophe Olivo-Marin[5], Bruno Antonny[1], Frank Lafont[3], Emmanuel Lemichez[2,*,‡] and Hélène Barelli[1,*,‡]

ABSTRACT

Metabolic studies and animal knockout models point to the critical role of polyunsaturated docosahexaenoic acid (22:6, DHA)-containing phospholipids (DHA-PLs) in physiology. Here, we investigated the impact of DHA-PLs on the dynamics of transendothelial cell macroapertures (TEMs) triggered by RhoA inhibition-associated cell spreading. Lipidomic analyses showed that human umbilical vein endothelial cells (HUVECs) subjected to a DHA diet undergo a 6-fold enrichment in DHA-PLs at the plasma membrane (PM) at the expense of monounsaturated oleic acid-containing PLs (OA-PLs). Consequently, DHA-PL enrichment at the PM induces a reduction in cell thickness and shifts cellular membranes towards a permissive mode of membrane fusion for transcellular tunnel initiation. We provide evidence that a global homeostatic control of membrane tension and cell cortex rigidity minimizes overall changes of TEM area through a decrease of TEM size and lifetime. Conversely, low DHA-PL levels at the PM lead to the opening of unstable and wider TEMs. Together, this provides evidence that variations of DHA-PL levels in membranes affect cell biomechanical properties.

KEY WORDS: Polyunsaturated phospholipids, Docosahexaenoic acid, DHA, Membrane fusion, Large-scale membrane dynamics, Endothelium, Transendothelial cell macroaperture, Bacterial toxin, Actin cytoskeleton

INTRODUCTION

The plasma membrane (PM) attached to the cortical cytoskeleton forms a composite material that undergoes constant reshaping to perform essential cellular processes, including cell division, migration and phagocytosis, and to maintain tight epithelial and semi-permeable endothelial barrier organization and function (Levayer and Lecuit, 2012; Salbreux et al., 2012). Lipidomic approaches offer ways to quantitatively decipher the impact of fine-tuned changes in the composition of lipid acyl chains on membrane dynamics.

Phospholipids (PLs) often contain an unsaturated acyl chain at the sn-2 position, which determines the biophysical properties of cellular membranes. Fatty acids (FAs) are classified as saturated, monounsaturated and polyunsaturated by the number of double bonds present in the hydrocarbon acyl chain. Several glycerophospholipid classes, including phosphatidylcholine (PC), phosphatidylethanolamine (PE) and phosphatidylserine (PS), are the dominant constituents of the PM in addition to cholesterol. Notably, phosphatidylcholine (PC) accounts for 40–50% of total phospholipids at the PM (van Meer et al., 2008). Variations in the length and number of double bonds in acyl chains lead to a remarkably large repertoire of phospholipid variants, such as PC(16:0/18:1), PE(18:0/20:4) and PS(18:0/22:6), which confer different biophysical properties, i.e. fluidity, packing order and curvature (Barelli and Antonny, 2016; Harayama and Riezman, 2018). The double bonds in polyunsaturated PLs allow acyl chains to twist at various angles, thereby providing the membrane with remarkably flexible properties (Manni et al., 2018). It is important to decode how the pattern of acyl chain variants in PLs translates into variations in cellular membrane dynamics (Harayama and Riezman, 2018; Pinot et al., 2014).

With 22 carbons and six double bonds, docosahexaenoic acid (DHA) is the most unsaturated form of the omega-3 FAs. Given the limited synthesis of this FA from linolenic acid, a dietary supply of DHA is essential for the functions of the retina (Shindou et al., 2017) and for spermatogenesis (Iizuka-Hishikawa et al., 2017) in addition to brain function (Bazinet and Layé, 2014). In particular, animals fed with polyunsaturated FA-free diets develop reduced visual functions paralleling the low DHA content in their retinas, outcomes that indicate the critical requirement of attaining DHA from the diet for visual function (Jeffrey and Neuringer, 2009). Lysophosphatidic acid acyltransferase 3 (LPAAT3; also known as AGPAT3), which catalyzes the esterification of DHA to generate phosphatidic acid and form precursors of PLs, notably DHA-containing PC and PE, is particularly rich in the retina and testis (Yuki et al., 2009). Mice with LPAAT3 knocked out display male infertility and show visual impairment due to structural defects in the membranes of photoreceptors. Much remains to be learned on how DHA impacts the architecture and dynamics of the PM.

Recent works have shown that polyunsaturated lipids facilitate membrane processes requiring deformations at the nanometer scale. First, incorporation of polyunsaturated acyl chains into PLs facilitates endocytosis in model cellular systems and makes the pure lipid bilayer more flexible and prone to fission mediated by dynamin and endophilin (Manni et al., 2018; Pinot et al., 2014). These effects might explain why polyunsaturated phospholipids (PUPLs) are necessary for proper synaptic vesicle formation

[1]Institut de Pharmacologie Moléculaire et Cellulaire, UMR 7275, CNRS and Université Côte d'Azur, 06560 Valbonne, France. [2]Institut Pasteur, Université de Paris, CNRS UMR6047, Inserm U1306, Unité des Toxines Bactériennes, 75015 Paris, France. [3]Université de Lille, CNRS, Inserm, CHU Lille, Institut Pasteur Lille, U1019 - UMR 9017 - CIIL - Center for Infection and Immunity of Lille, F-59000 Lille, France. [4]Université de Lorraine, LCP-A2MC, F-57000 Metz, France. [5]Institut Pasteur, BioImage Analysis Unit, CNRS UMR 3691, Paris, France.
*These authors contributed equally to this work

‡Authors for correspondence (emmanuel.lemichez@pasteur.fr; helene.barelli-vincent@inserm.fr)

L.F., 0000-0001-9452-8188; D.G.-R., 0000-0001-6152-2222; C.M., 0000-0001-8521-2990; A.M., 0000-0003-1453-6482; D.D., 0000-0003-2807-9198; S.D., 0000-0002-2204-7083; J.C.O.-M., 0000-0001-6796-0696; B.A., 0000-0002-9166-8668; F.L., 0000-0001-8668-2580; E.L., 0000-0001-9080-7761; H.B., 0000-0001-6376-863X

Handling Editor: James Olzmann
Received 15 July 2021; Accepted 27 November 2021

Journal of Cell Science (2022) 135, jcs259119. doi:10.1242/jcs.259119

(Tixier-Vidal et al., 1986). Second, polyunsaturated phosphatidic acid facilitates secretory granule exocytosis in neuroendocrine chromaffin cells, probably by stabilizing intermediates that contribute to a high-curvature membrane during fusion pore formation (Tanguy et al., 2020). Finally, PUPLs modulate the activity of several mechanosensitive ion channels, including TRP, TRP-like and Piezo channels (Caires et al., 2017; Randall et al., 2015; Romero et al., 2019). Many of these effects have been proposed to arise from a reduction in the energetic cost of membrane bending and/or from a modulation of the energy required for protein conformational changes within the membrane matrix. However, whether and how the enrichment of cellular membranes with PUPLs modulates large-scale membrane dynamics remain to be elucidated.

Transcellular pores are observed in endothelial cell-lined vessels and form during the transcellular diapedesis of leukocytes (Aird, 2007; Braakman et al., 2016; Schimmel et al., 2017). Several toxins from pathogenic bacteria, such as RhoA-inhibitory exoenzymes from *Staphylococcus aureus* and *Clostridium botulinum,* can induce transendothelial cell macroaperture (TEM) tunnels (Lemichez et al., 2013). This TEM formation has been linked to increased vascular permeability and dissemination of *S. aureus* in tissues via the hematogenous route (Boyer et al., 2006; Munro et al., 2010; Rolando et al., 2009). Several bacteria secrete toxins that lower cell actomyosin contractility, thereby promoting cell spreading, which favors close contact between the dorsal and basal membranes and initiates their self-fusion (Boyer et al., 2006; Ng et al., 2017). This step of fusion between the basal and dorsal membranes determines the very first step of TEM creation, hereafter named nucleation. The cellular dewetting physical model is based on the premise that spreading cells generate enough membrane tension for TEM nucleation and growth (Gonzalez-Rodriguez et al., 2012). Widening of TEMs is resisted by line tension, which is partially explained by the membrane curvature generated by torus-like pores (Gonzalez-Rodriguez et al., 2012). After nucleation, an imbalance between the membrane and line tension causes TEMs to passively expand up to the maximal equilibrium size, which is stabilized by a newly formed stiff actomyosin cable that encircles TEMs (Stefani et al., 2017). TEMs are eventually sealed by active cytoskeleton-based processes (e.g. lamellipodia formation or purse-string contraction). Although considerable progress has been made in understanding the interactions between the membrane and actin cytoskeleton regulatory machinery in the control of TEMs, much remains to be determined about the contribution of PM mechanical properties.

We investigated these areas by analyzing TEM dynamics in primary human endothelial cells subjected to polyunsaturated versus monounsaturated FA diets. We show that membrane enrichment in DHA-containing PLs (DHA-PLs) increases the probability of TEM nucleation while decreasing the width and the lifetime of transcellular tunnels leading to conservation of cumulative TEM area. Moreover, we show that impoverishment in DHA-PLs has a detrimental impact on TEM stability.

RESULTS

Comprehensive analysis of the PLs in HUVECs fed with different FA diets

Recent progress has revealed the importance of whole-cell lipidome adaptation to massive incorporation of polyunsaturated FAs in order to maintain cellular viability (Levental et al., 2020). In contrast, little is known about how different cell types adapt their PM composition to a PUPL increase, and whether these adaptations fully preserve biomechanical properties of PM attached to the underlying cortical cytoskeleton network.

Since endothelial cells are physiologically submitted to direct variations of dietary FA chains in plasma, we performed comprehensive lipidome analyses of HUVECs, for total membranes and purified PM, submitted to DHA (C22:6) versus OA (C18:1) diets, i.e. the most polyunsaturated acyl chain versus the most abundant monounsaturated acyl chain in PLs, respectively (Harayama and Riezman, 2018). HUVECs were first subjected to medium containing lipoprotein-depleted serum (LPDS) followed by a diet of LPDS supplemented with bovine serum albumin (BSA) complexed either with DHA (C22:6) or OA (C18:1). Lipidome analysis was then conducted by comparing relative quantities of lipid species using a Q Exactive mass spectrometer.

While lipid starvation conditions decreased the triglyceride (TG) storing form of acyl chains, we did not detect significant difference in the relative distribution of phospholipid classes (Fig. 1A; Fig. S1A–C). We monitored the cellular lipidome of HUVECs fed with the different FA diets for different times. We recorded a massive increase in TG that peaked at 1 h (Fig. S2A). The incorporation of FAs into phospholipids occurred with slower kinetics (Fig. S2B–D), reaching a plateau at 6 h, most notably for DHA incorporation into PC (Fig. S2B). Importantly, the relative distribution of PL classes was conserved between conditions, except for PE, which was reduced by 25% in the DHA-treated cells (Fig. 1A).

As shown in Fig. 1B and Fig. S1B, in contrast to what was seen with the OA diet, the DHA diet had an impact on the profile of PLs, which show enrichment in DHA-PL species. Specifically, DHA was incorporated in large amounts into PC and PE, with a 4-fold increase in PC(16:0/22:6) and a 2-fold increase in PE(18:0/22:6) (Fig. 1B). In comparison, the remodeling of the anionic lipids PS and phosphatidylinositol (PI) was modest, although we recorded an increase in PI(18:0/22:6) at the expense of PI(18:1/20:4), one of the major PI species. In sharp contrast, OA treatment had a slight impact on the acyl chain profile of phospholipids, inducing a specific increase in PLs (18:1/18:1) at the cellular level, which was largely restricted to PC (Fig. 1B). Overall, cells fed with DHA displayed considerable enrichment in PUPLs, which we estimated as a polyunsaturated PC increase from 22% to 47%, at the expense of OA-containing PC (Fig. 1C; Fig. S2D). Furthermore, the addition of OA to HUVECs had a minor impact on the lipidome, which was already rich in OA-containing PLs and poor in DHA-containing lipids.

Shifting the PM PL balance from the monounsaturated to the hexa-unsaturated form

The acyl chain profile of PLs varies according to subcellular localization (Antonny et al., 2015). Thus, we determined the impact of the OA and DHA FA-diet conditions on the composition of PLs at the PM. For this experiment, we prepared giant plasma membrane vesicles (GPMVs), corresponding to PM blebs (Fig. 2A). We observed the expected enrichment of the PM markers annexin II and Na^+/K^+ ATPase in the GPMV fractions (Fig. 2B). Markers of internal compartments were observed in the total cell membrane fractions, but were largely excluded from the GPMV fractions. The lipidomic analysis of the GPMVs compared to that of the total membrane fractions showed an enrichment in PS and sphingomyelin (SM), which are known to concentrate in the PM (Fig. 2C). In contrast, lipids characterizing membranes of internal compartments, such as diglyceride (DG; ER and lipid droplets) and lysobisphosphatidic acid (LBPA; late endosomes), were largely excluded from the GPMV

Journal of Cell Science (2022) 135, jcs259119. doi:10.1242/jcs.259119

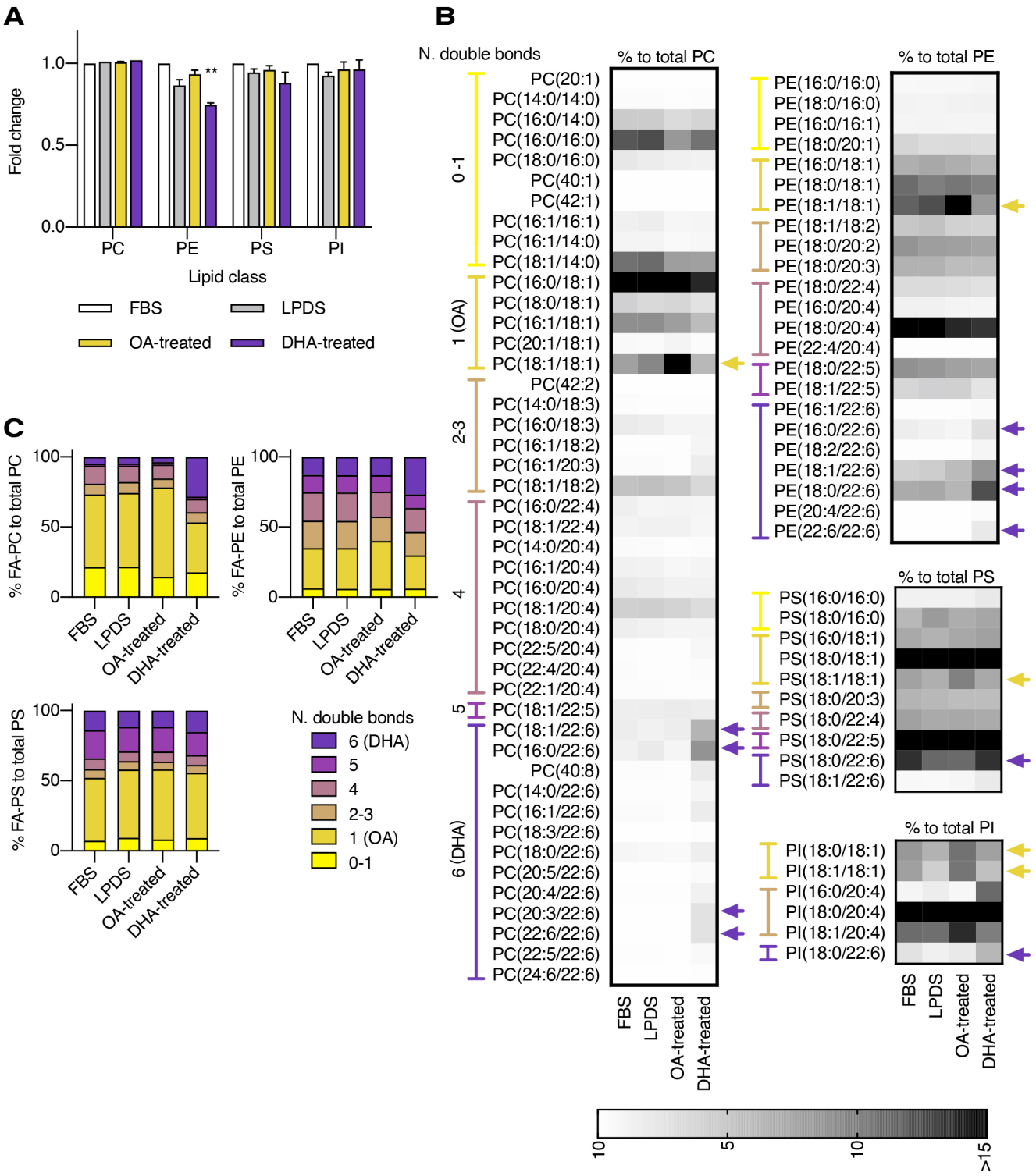

Fig. 1. Analysis of PL classes in HUVECs submitted to OA versus DHA conditions. (A) Global fold change of phosphatidylcholine (PC), phosphatidylethanolamine (PE), phosphatidylserine (PS) and phosphatidylinositol (PI) classes from HUVECs submitted to a OA- or DHA-diet for 6 h compared to FBS- or LPDS-cultured HUVECs. ***P*<0.01 compared to FBS-treated cells (one-way ANOVA with Bonferroni corrections); no mark indicates result is not significantly different from FBS-treated cells. (B) Lipidic profiles comparison of the different PL class (PC, PE, PS and PI) upon OA-diet or DHA-diet compared to controls (FBS and LPDS). PC with unseparated sn-1 and sn-2 acyl chains represent less than 5% of total PC. Values were normalized individually to the sum of each PL class. Purple arrows indicate increases in PL species containing a 22:6 (DHA) acyl chain, whereas yellow arrows indicate decreases in PL species containing an 18:1 (OA) acyl chain. (C) PL species distribution regarding their number of double bond (level of unsaturation): from zero to six double bonds as illustrated in Fig. 1B. OA and DHA contain one and six double bonds, respectively. FBS, fetal bovine serum; LPDS, lipoprotein-depleted serum. Data show means ±s.e.m. for *n*>3 experiments; three biological replicates.

Journal of Cell Science (2022) 135, jcs259119. doi:10.1242/jcs.259119

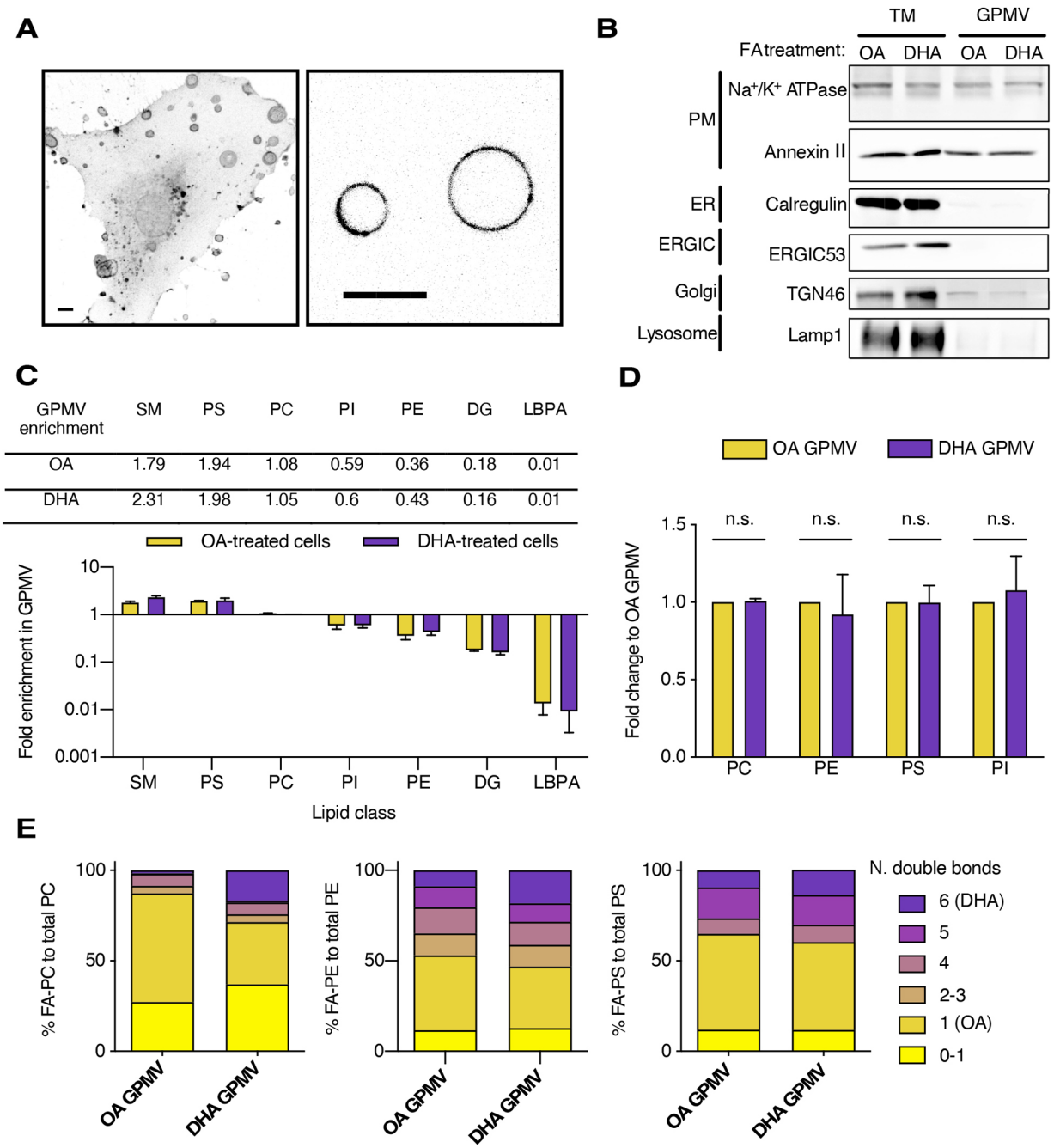

Fig. 2. Lipidomic analysis of phospholipids from GPMVs. (A) 3D-projection of WGA–Alexa488-labeled GPMVs (left) and FM4-64-labeled GPMVs (right) from HUVECs. Data are representative of three repeats. Scale bars: 10 µm. (B) Western blot of total membrane (TM) and GPMV fractions for different organelle markers. Equal amounts of proteins for TM or GPMV were loaded. Plasma membrane (PM) markers, Na^+/K^+ATPase and annexin II; Endoplasmic reticulum (ER) marker, calregulin; ER-Golgi intermediate compartment (ERGIC) marker, ERGIC53; Golgi complex marker, trans-Golgi network 46 (TGN46); lysosome marker: lysosomal-associated membrane protein 1 (LAMP1). Data are representative of three repeats. (C) Lipidomic analyses of GPMVs from OA- or DHA-treated cells. Lipid class enrichment in GPMVs was calculated by dividing the relative content of each lipid class in GPMVs by those of total membranes. Values bigger than 1 indicate that lipids were enriched in GPMVs; values smaller than 1 indicate that lipids were excluded from GPMVs. SM, sphingomyelin; PC, phosphatidylcholine; PE, phosphatidylethanolamine; PS, phosphatidylserine; PI, phosphatidylinositol; DG, diacylglycerol; LBPA, lysobisphosphatidic acid. (D) Fold change of different PL classes in DHA-treated cells compared with OA-treated cells. not significant (n.s.; unpaired two-tailed Student's *t*-test). (E) PL species distribution regarding their number of double bond (level of unsaturation): from zero to six double bonds as illustrated in Fig. 1B. OA and DHA contain one and six double bonds, respectively. Data in C–E show mean±s.e.m.; $n>3$ experiments; three biological replicates.

fractions (Fig. 2C). Moreover, quantitative analysis of PL classes in the GPMV fraction established the conservation of PL class distribution at the PM, including PE (Fig. 2D).

We analyzed the changes in the acyl chain composition of PLs in the PM-derived GPMVs prepared from cells subjected to the two FA diets. As observed for the total membrane fraction, the GPMV fraction from DHA-treated cells was enriched in DHA-containing PC, the dominant PL class, by 10-fold (from 1.6% to 16.7%) and PE species by 2-fold (from 8.8% to 18.2%) at the expense of monounsaturated species, as compared to GPMV from

Journal of Cell Science (2022) 135, jcs259119. doi:10.1242/jcs.259119

OA-treated cells (Fig. 2E). Thus, the DHA diet triggered a 1.9-fold reduction in OA-containing PC compared with that seen in OA-treated cells. Interestingly, these variations are accompanied by an increase in saturated PC species in agreement with recent work by Levental et al. (2020).

Our comprehensive analysis of the HUVEC lipidome establishes that these cells have a PM intrinsically rich in OA-containing PLs, a profile that can be largely shifted towards polyunsaturated DHA-PLs upon exposure to a high-DHA FA diet.

The DHA diet leads to smaller pores in the TEM population

Inhibition of the small GTPase RhoA by bacterial ExoC3-like toxins induces the nucleation and expansion of TEMs (Boyer et al., 2006). The nucleation and growth of TEMs are triggered by a collapse of RhoA-driven actomyosin contractility that leads to a spreading of cells and a reduction of their thickness (Ng et al., 2017) (Fig. 3A). We first verified that modification of RhoA signaling had no impact on the proper incorporation of OA or DHA into PLs (Fig. S3A,B). To this end, HUVECs were incubated in LPDS medium as the sole treatment or in LPDS containing the RhoA-inhibitory C3-exoenzyme (ExoC3). Next, cells were incubated for 1 to 6 h in LPDS medium supplemented with BSA complexed with either OA or DHA FAs. We set a treatment of 24 h with ExoC3 prior to DHA/OA incorporation to avoid possible interference of fatty acyl chains incorporation on toxin endocytosis and translocation to the cytosol. To verify ExoC3 action on RhoA in all experimental conditions, we performed sequential ADP-ribosylation experiments showing that RhoA from ExoC3-treated cells becomes refractory to the second step of ADP-ribosylation performed *in vitro* (Fig. S3C). In parallel, we observed a disruption of actin stress fibers due to ExoC3 action under the different diet conditions (Fig. 3B).

We analyzed the impact of OA or DHA treatment on the spreading of cells induced by ExoC3. Measures of cell area showed no significant difference between the two diet conditions in cells without ExoC3 (Fig. 3C). When cells were treated with ExoC3, we recorded a 1.2-fold spreading of both OA- and DHA-treated cells, indicating that enrichment in DHA-PLs in the HUVECs did not significantly influence the extent of their spreading in response to the inhibition of RhoA.

Next, we analyzed TEM parameters on fixed cells stained with FITC–phalloidin to label filamentous actin accumulating around TEMs. We observed that ∼25% of cells displayed at least one TEM with no significant difference between cells cultured under the two FA diet conditions (Fig. 3D). Interestingly, we recorded a significant increase in the density of TEMs per cell in the DHA condition to 3.5±0.3 TEM/cell (mean±s.e.m.) versus 2.5±0.1 TEM/cell for the OA-fed cells (Fig. 3E). The increase of TEM density was accompanied by a decrease of the median TEM area in the DHA-treated cells compared with the OA-treated cells, with area $(A)_{DHA}$=5.6 µm^2 versus A_{OA}=9.9 µm^2, respectively (Fig. 3F,G). Consistent with this, analysis of the distribution of the size of TEMs showed that the DHA diet induced a major shift toward TEMs of smaller size [radius (R)<1 µm; 21% to 33%] at the expense of larger TEMs (R>4 µm; 24% to 14%) (Fig. 3H). This first set of data reveals that inhibition of RhoA and incorporation of DHA into PLs did not interfere with each other, whereas the incorporation of DHA affects the TEM biomechanical parameters of density and size.

The DHA diet increases TEM nucleation frequency

TEM tunnels form labile openings (Fig. 4A; Movie 1). After nucleation and growth, TEMs reach a stable state in which they oscillate around a maximal area. After this period of latency, TEMs undergo a phase of closure via actin-dependent processes involving either purse-string contraction or membrane wave extension (Maddugoda et al., 2011). Here, we noticed that ∼70% of the TEMs resealed via a purse-string contraction phenomenon regardless of the FA diet (data not shown).

To quantitatively analyze TEM dynamics, we recorded the cycles of TEM opening and closing by time-lapse video in LifeAct–GFP-expressing cells, allowing us to determine the frequency of TEM nucleation and their complete lifetime. Strikingly, this revealed a critical impact of the DHA FA diet on the mechanical control of TEM dynamics. Fig. 4B shows that the DHA-fed cells had a higher frequency of opening events during the recording period than OA-fed cells (Movies 2 and 3). Mean values were N=19.3 events/h for the DHA-fed cells versus N=8.9 events/h for the OA-fed cells (Fig. 4C). Consistent with the impact of DHA on the distribution of TEM sizes, we found that the lifetime for complete TEM opening and closing cycle was 1.7-fold shorter in the DHA-fed cells than in OA-fed cells, i.e. mean values of 24.6±1.8 min for the DHA-fed cells versus 42.0±4.0 min for the OA-fed cells (Fig. 4D). TEM cycles encompass dynamic phases of opening and of closure, as well as a phase of latency where the TEM area oscillates within ∼5% of its maximal size (Fig. S4A). While the time for TEM opening was not affected by DHA, we recorded a decrease in the duration of both the latency and closure phases (Table 1). The probability of observing a TEM in a cell depends on the product of TEM nucleation frequency by their lifetime. Despite differences in the opening frequency of TEMs, we have recorded an average conservation in the total TEMs area between OA and DHA conditions. This conservation is interpreted as a consequence of the reduction in the overall lifetime of TEMs. Together, our data reveal a striking mechanical coupling between the nucleation rate of TEMs and their lifetimes, which accounts for the observed higher rate of opening of TEMs of smaller size upon membrane enrichment in DHA-PLs (Fig. S4B).

The DHA diet decreases cell thickness

We further investigated whether RhoA inhibition and DHA enrichment would affect the cortical elasticity of cells. We used atomic force microscopy (AFM) force mapping with a small colloidal-shaped tip to probe the first 40 nm layer of cell elasticity in the perinuclear region of living cells (Fig. 5A). RhoA inhibition greatly reduced the Young's modulus, by 1.7-fold, as reported previously (Ng et al., 2017). However, we measured similar elasticity in cells subjected to OA and DHA treatments [5.1±0.2 kPa versus 5.8±0.3 kPa, respectively; median±range (minimum to maximum); n=40 TEMs] (Fig. 5C), suggesting that there is only a negligible impact of DHA enrichment on cortical elasticity. Nor did we observe any significant modification in the homogeneity of elasticity (Fig. 5B).

We later measure the topography of the cell thickness at the periphery of TEMs. This was performed using a force feedback imaging mode and computing the zero-force topographical image on fixed, intoxicated cells, with a sharp tip. Cells with TEM showing no fluorescent actin ring were selected. Interestingly, DHA treatment decreased the cell thickness to 1.2-fold; i.e. mean values for the DHA-fed cells was 164±6 nm versus 190±6 nm for the OA-fed cells (Fig. 5D,E). As previously reported, the TEM rim is elevated and forms a ridge structure (Maddugoda et al., 2011). In accordance with the measures of cell thickness, the height of the TEM ridge was decreased 1.2-fold in the DHA-enriched cells

Journal of Cell Science (2022) 135, jcs259119. doi:10.1242/jcs.259119

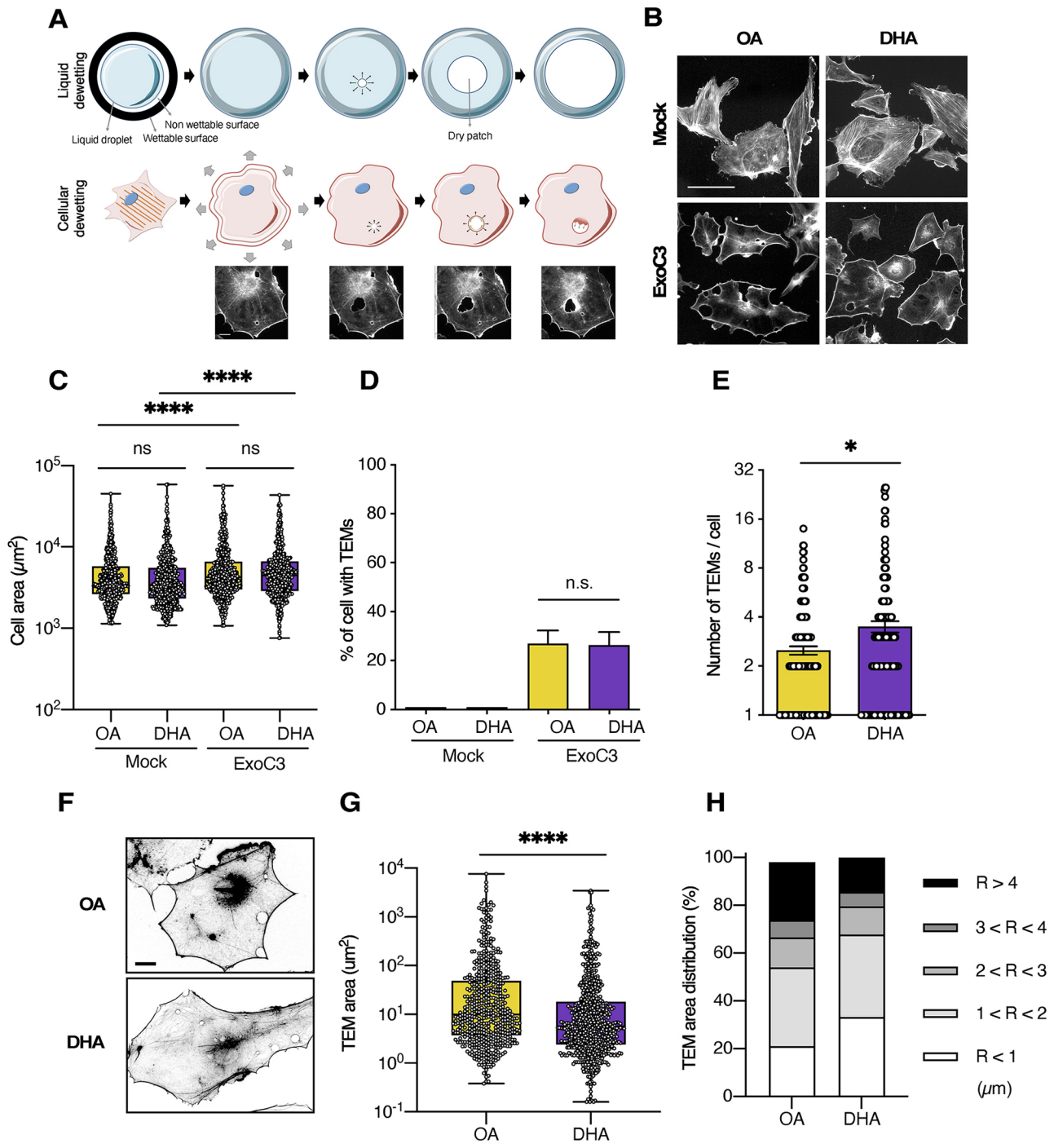

Fig. 3. The impact of DHA on TEM parameters. (A) Schematic representations of liquid dewetting physics phenomenon and TEM dynamics. Scale bar: 20 µm. (B–H) HUVECs were treated with C3 exoenzyme or without (Mock) for 16 h prior to 6-h fatty acid diet (OA or DHA) as sole source of exogenously added acyl chain. (B) FITC–phalloidin staining of HUVEC in Mock, OA or DHA conditions. Data are representative of three repeats. Scale bar: 100 µm. (C) Cell area of cells on OA or DHA diet. The box represents the 25–75th percentiles, and the median is indicated. The whiskers show the range (minimum to maximum); cells >450/experiment; two biological replicates. (D) Percentage of HUVEC with at least one TEM in the population in OA or DHA conditions. Data show means±s.e.m.; cells >200/experiment; three biological replicates. (E) Number of TEMs per cell under OA or DHA diet. Data show median±range of >150 cells from three independent experiments (>50 cells/experiment). (F) Representative FITC–phalloidin staining of OA or DHA-treated cells intoxicated with C3 toxins. Data are representative of three repeats. Scale bar: 20 µm. (G) Graph shows median values of TEM area in fixed cells treated with either OA or DHA. The box represents the 25–75th percentiles, and the median is indicated. The whiskers show the range (minimum to maximum); of >450 TEMs from 3 independent experiments (>40 cells/experiment). (H) Distribution of TEM sizes in HUVEC under OA- or DHA-diet. *P<0.05; ****P<0.0001; n.s., not significant (nonparametric Mann–Whitney statistical test).

(Fig. 5F). We concluded that DHA enrichment decreases the thickness of TEMs without affecting the cell elasticity contributed by the cellular cortex (Fig. 5B–G).

The impact of DHA-PL enrichment on TEM opening kinetics

The dynamics of TEM opening were analyzed with a custom-made Icy-based program that automatically segments the LifeAct–GFP-

Journal of Cell Science

Journal of Cell Science (2022) 135, jcs259119. doi:10.1242/jcs.259119

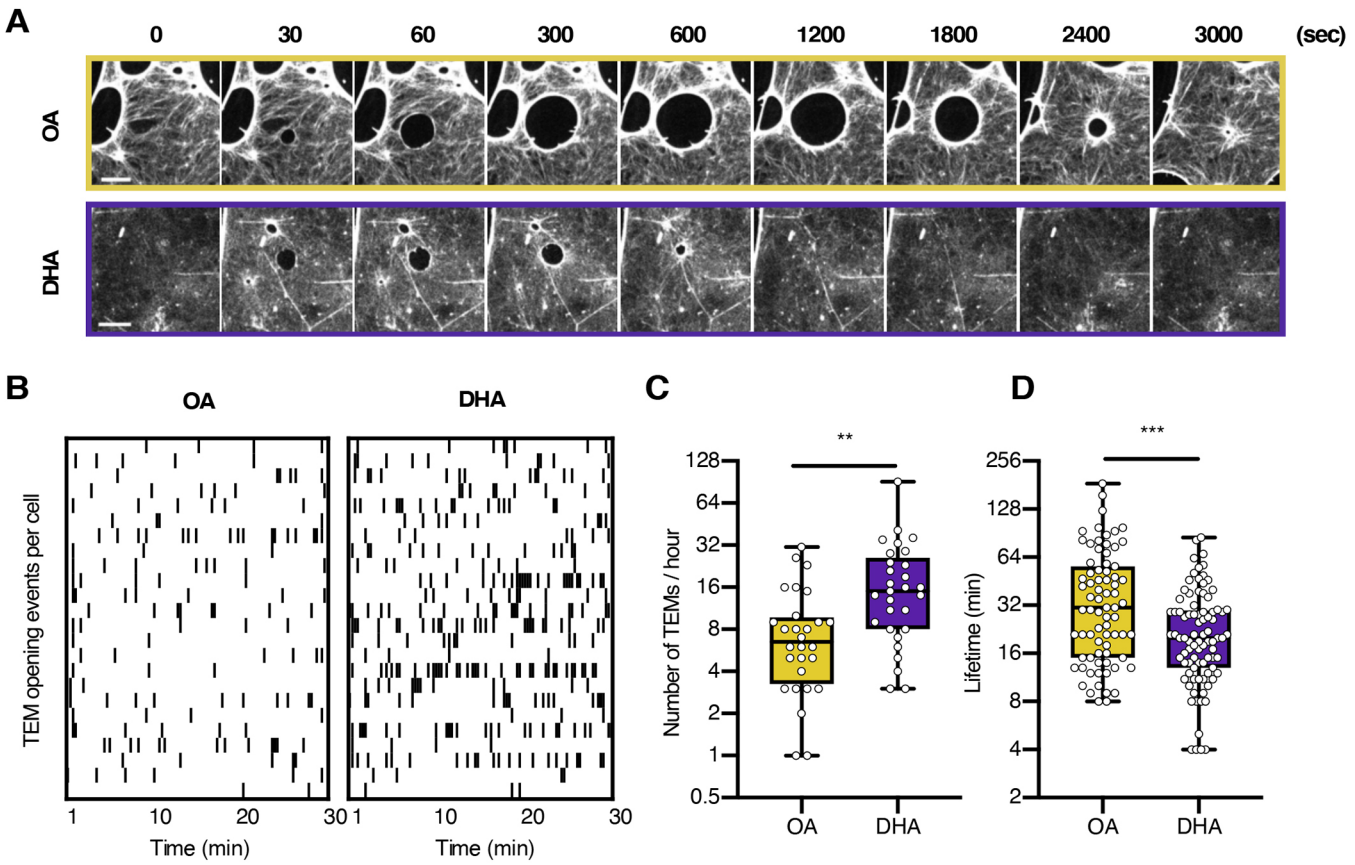

Fig. 4. Impact of DHA-enriched membrane on TEM opening dynamics. (A) Time-lapse images of TEM opening dynamics in OA- or DHA-fed cells using LifAct–GFP as a label. Data are representative of 28 repeats. Scale bars: 10 µm. (B,C) Frequency of TEM opening events per cell in cells treated with ExoC3 and fed with either OA or DHA. (B) Each row on the *Y*-axis of the diagram pinpoints all opening events of TEM in a single cell, each black bar is an individual opening event. (C) Graph showing total number of TEM opening events per cell per hour. Data shown are median±range (minimum to maximum); n>28 cells from 28 independent experiments. (D) Graph shows the distribution of values of TEM opening lifetimes measured for each TEM. The box represents the 25–75th percentiles, and the median is indicated. The whiskers show the range (minimum to maximum); n>75 TEMs from >8 independent experiments. **P<0.01; ***P<0.001 (Mann–Whitney statistical test).

decorated actin-rich circumference of TEMs as a function of time (Figs 4A and 6A). This analysis enabled us to study the dynamics and maximal size of parameters of single TEMs.

Interestingly, we observed that, under LPDS conditions, ∼11% of the TEMs in the OA-treated cells versus 3% of the TEMs in the DHA-treated cells (Fig. S5D) resumed their enlargement 104±33 s (mean±s.e.m.) after stabilization (i.e. after they had reached the first stable state as illustrated in Fig. S5A,B and Movie 4), suggesting that DHA-PL-rich membranes form pores with greater stability (Fig. S5C,D). In parallel, we performed a comparative super-resolution stimulated emission depletion (STED) microscopy analysis of the actin structures around the TEMs in the OA- and DHA-fed cells; i.e. we examined the typical actomyosin belt and membrane wave-containing dendritic F-actin (Stefani et al., 2017). No significant difference in actin organization around the TEMs between the two conditions was recorded (Fig. 6B).

For the quantitative analysis described in the workflow in Fig. 6A, we focused on the initial growth up to the first equilibrium state reached by the TEMs, a regime that can be directly compared to predictions of the cellular dewetting physical model, which describes TEM dynamics (Gonzalez-Rodriguez et al., 2012). We recorded and defined the median size of the TEMs over the recording period (Fig. 6C). According to the cellular dewetting model, the initial speed of TEM opening is primarily dictated by membrane tension while at later timings opening speeds progressively integrate forces due to cytoskeleton remodeling along the edge of TEMs (Stefani et al., 2017). A comparative analysis of the initial speeds of opening between 10 and 20 s (V_i) in the OA- and DHA-fed cells revealed no significant difference

Table 1. Summary of TEM measurements presented in the figures

	OA	DHA	Statistics
Cell area (µm^2)	6330±271	6003±251	ns
Cell thickness (nm)	190±6	164±6	**
% of cells with TEMs	27±3	26±3	ns
Number of TEMs/cell	2.5±0.1	3.5±0.3	*
TEM frequency (TEMs/h)	8.9±1.4	19.3±3.2	**
TEM max size (µm^2)[a]	37.4 (27.6–59.4)	25.4 (21.2–28.6)	*
Opening time (sec)	179±21	162±23	ns
Initial opening speed (µm^2/s)[a]	0.47 (0.35–0.95)	0.39 (0.29–0.54)	ns
Late opening speed (µm^2/s)[a]	0.38 (0.22–0.61)	0.27 (0.14–0.37)	*
Latency phase (min)	7.3±0.6	5.3±0.4	*
Closure time (min)	16.3±1.4	11.1±0.8	**
Closure speed (µm^2/s)[a]	4.3 (3.4–6.1)	2.7 (2.1–3.3)	***
Lifetime (min)	42.0±4.0	24.6±1.8	***

Data show the means±s.e.m. except where indicated by 'a' , where the median (95% c.i., upper–lower) is shown.
ns, not significant; *P<0.05; **P<0.01; ***P<0.001 (Mann–Whitney test).

Journal of Cell Science (2022) 135, jcs259119. doi:10.1242/jcs.259119

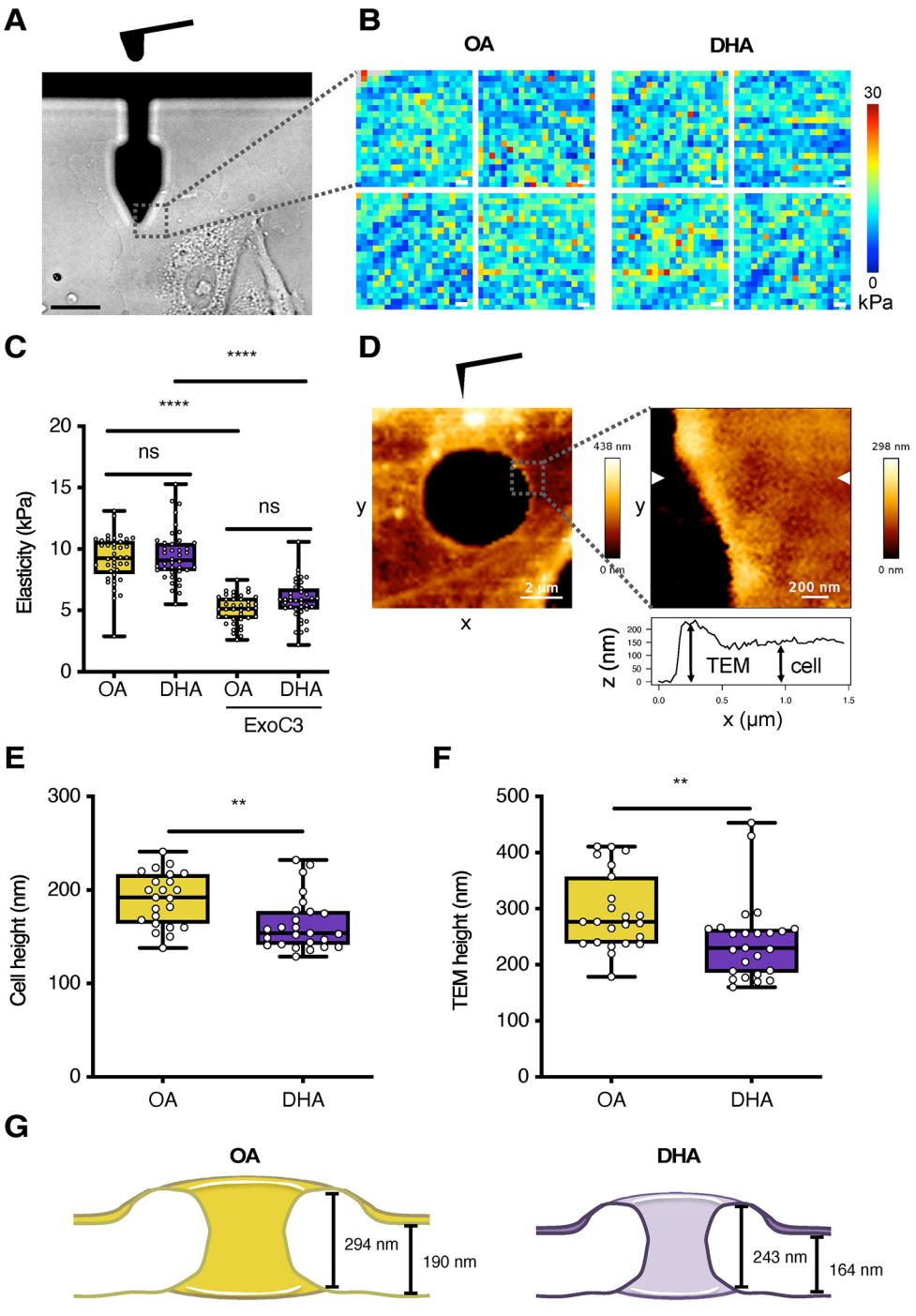

Fig. 5. Impact of DHA on cell geometry. (A) Atomic force microscopy (cantilever shape seen in the foreground) is used to measure the mechanical parameters of the cell (background in bright field). Scale bar: 20 µm. (B) Heatmap of cell elasticity (kPa) on OA- and DHA-treated cells. Scale: 10 µm^2 per field of view. (C) Graph showing the cortical elasticity of Mock or ExoC3-intoxicated cells treated with OA or DHA. The box represents the 25–75th percentiles, and the median is indicated. The whiskers show the range (minimum to maximum); *n*=40 TEMs. Data showed a Gaussian distribution. ****P<0.0001; n.s., not significant (one-way ANOVA with Bonferroni correction). (D–F) AFM zero-force topography measurement (D) of the cell thickness at the periphery of TEMs (E) and thickness of TEMs border (F) were measured by AFM using zero-force topography. In E,F, the box represents the 25–75th percentiles, and the median is indicated. The whiskers show the range (minimum to maximum); *n*>20 TEMs. **P<0.01 (Mann–Whitney statistical test). (G) Diagram showing the mean curvature of TEMs derived from the TEM height measurements.

between the DHA-fed cells ($V_{i\text{-}DHA}$=0.39 µm^2 s^{-1}) and OA-fed cells ($V_{i\text{-}OA}$=0.47 µm^2 s^{-1}) (Table 1). In contrast, when we compared the median of late opening speeds over the first 20–70 s (V_0), the values were 1.4-fold lower for the DHA-fed cells ($V_{0\text{-}DHA}$=0.27 µm^2 s^{-1}) than for the OA-fed cells ($V_{0\text{-}OA}$=0.38 µm^2 s^{-1}) (Fig. 6D). The cellular dewetting model implies that the nucleation and initial TEM opening speed (at the very first opening stage) are proportional to the membrane tension (Gonzalez-Rodriguez et al., 2012). Because the initial speed was similar between the OA- and DHA-treated cells, the average cell membrane tension is expected to be comparable between the two conditions. This conclusion is further supported by the observation of comparable spreading of the OA- and DHA-fed cells, because the cell spreading area correlates with cell membrane tension and TEM opening (Braakman et al., 2014).

In parallel, we assessed the maximal size of the TEMs during the recording periods. Consistent with measures of the fixed cells, the TEM maximal size (S_{max}) was decreased by ∼1.5-fold in the DHA-treated cells compared with the OA-treated cells, with $S_{max\text{-}DHA}$=25.4 µm^2 versus $S_{max\text{-}OA}$=37.4 µm^2 (median values; see Table 1; Fig. 6E). In accordance with data on fixed cells, we recorded, in live cells, an increase in small (R<3 µm) TEMs from 38% to 60% at the expense of large (R>4 µm) TEMs (from 42% to 20%) in the DHA-treated cells versus OA-treated cells (Fig. 6F). Consistent with the concomitant decrease of TEM size and speed of opening, we recorded for the DHA-fed cells no difference in the

Journal of Cell Science (2022) 135, jcs259119. doi:10.1242/jcs.259119

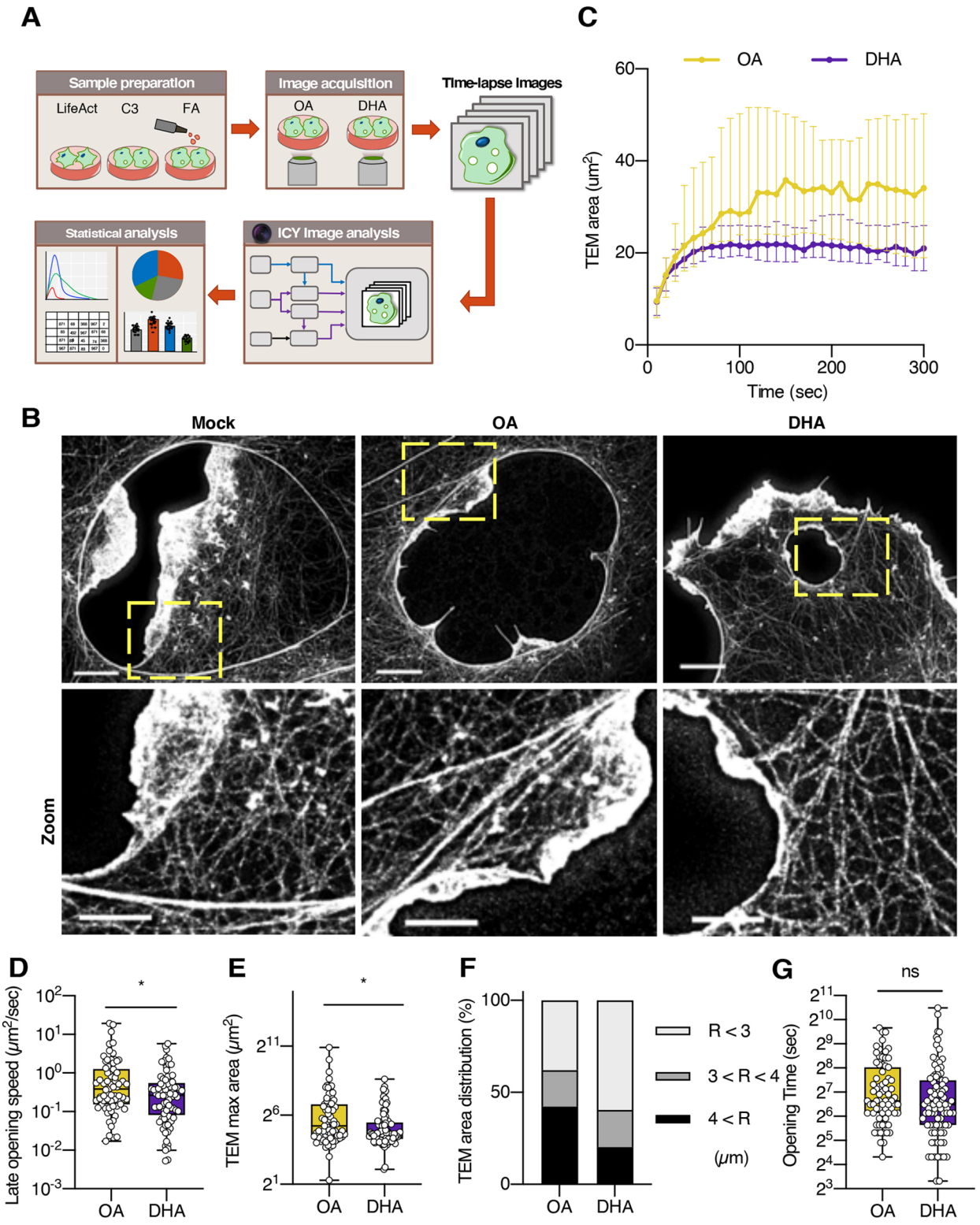

Fig. 6. Impact of DHA-enrichment on TEM opening parameters. (A) Experimental workflow. HUVECs cultivated in LPDS medium were transfected with LifeAct–GFP, treated with C3 toxin, and fed with OA- or DHA-BSA for 6 h. The dynamics of each TEM was recorded by spinning disk confocal microscopy and was analyzed through a custom Icy-based protocol. (B) Super-resolution stimulated emission depletion (STED) microscopy images of phalloidin-StarRed in C3 intoxicated cells treated without any fatty diet (Mock) or with OA- or DHA-diet. Scale bar: 5 µm (upper) and 2 µm (lower). Data are representative of three repeats. (C) Graph showing median values of TEM area as a function of time in cells treated with either OA (yellow, *n*=71 TEMs) or DHA (purple, *n*=94 TEMs) as sole source of exogenously added acyl chain. Values correspond to average surface of TEMs. Data show median±95% c.i. from 28 independent experiments. (D) Distribution of opening speed of TEM between 20 s and 70 s. (E) Graph shows median values of TEM maximum area in cells treated with either OA or DHA. (F) Distribution of TEM sizes in HUVECs under OA or DHA diet. (G) Graph shows distribution of time durations to reach 95% of maximum area. (D,E,G) The box represents the 25–75th percentiles, and the median is indicated. The whiskers show the range (minimum to maximum); *n*>70 TEMs for each condition from 28 independent experiments. **P*<0.05; n.s., not significant (Mann–Whitney test).

Journal of Cell Science (2022) 135, jcs259119. doi:10.1242/jcs.259119

time to reach the maximal surface area, i.e. 179±21 s for the OA-fed cells and 162±23 s for the DHA-fed cells (Fig. 6G). Although DHA-PLs had no impact on the initial speed of opening, they reduced the overall TEM opening speed, thereby impacting the maximal TEM size.

The observed decrease in TEM size upon DHA enrichment is in apparent contradiction with a naïve prediction of the cellular dewetting physical model. Indeed, DHA enrichment has been reported to reduce membrane bending rigidity, as measured locally by pulling a membrane tube (Pinot et al., 2014). According to the cell dewetting model, a reduction of membrane bending rigidity would slow down the dynamics of membrane tension relaxation, which should lead to larger TEMs. This apparent contradiction is solved by realizing that TEM opening dynamics are controlled by an effective cortical bending rigidity, which results from joint membrane and cortex properties. According to the physical model, an estimate of this effective membrane bending rigidity is given by

$$\kappa \approx \frac{k_B T A_{\mathrm{cell}}}{8\pi N A_{\mathrm{max}}},$$

where N is the number of TEMs simultaneously evident per cell, A_{max} is the maximum area of a TEM, k_B is the Boltzmann constant, T is the temperature, and A_{cell} is the total cell spreading area (see Materials and Methods for details). This equation is based on the relaxation of membrane tension during TEM opening, as described by Helfrich's law (Helfrich, 1973). Membrane relaxation is larger when the bending rigidity κ is larger. In deriving this equation, we assume a joint effect of N, the number of simultaneous TEMs on membrane, on tension relaxation, which affects each TEM. Because the cell spreading area A_{cell} is the same in the OA- and DHA-fed conditions, this equation indicates that the effective bending rigidity κ is inversely proportional to the product $N{\cdot}A_{\mathrm{max}}$. A comparison between the two conditions leads to

$$\frac{\kappa_{\mathrm{DHA}}}{\kappa_{\mathrm{OA}}} \approx \frac{N_{\mathrm{OA}} \cdot A_{\mathrm{max,OA}}}{N_{\mathrm{DHA}} \cdot A_{\mathrm{max,DHA}}} = 1.05,$$

whose difference from 1 is not statistically significant. Thus, this calculation suggests that the average effective bending rigidity at the cellular scale is similar between cells in the OA- and DHA-fed conditions.

Overall, the interpretation of the experimentally observed TEM dynamics in light of the physical model suggests that average tension and effective bending rigidity, arising from membrane and cortex association that behaves as a composite material, are unchanged in cells subjected to these OA and DHA treatments. This result points to a regulation mechanism of global membrane dynamics controlling TEM opening that is robust despite changes in membrane lipid composition, which dictates the TEM nucleation rate.

DISCUSSION

Since the discovery of the cellular dewetting phenomenon, the contribution of PM mechanical properties to the dynamics of TEMs remains to be elucidated. Here, we show that the DHA FA diet induces a shift in the acyl chain composition of phospholipids at the PM of endothelial cells, with an increase in DHA-PLs, and greatly affects TEM dynamics. Remarkably, DHA-PL enrichment changes membrane dynamics, i.e. nucleation and lifetime of TEMs, in a coordinated manner to ensure the relative conservation of the overall TEM area per cell, and shifts the size range of the TEMs to a smaller range via reduction of opening speed. Moreover, DHA-PL enrichment reduced uncontrolled resumed TEM growth. Collectively, these findings indicate that DHA-PLs facilitate the nucleation of smaller TEMs displaying shorter lifetimes. Conversely, deficient DHA-PLs may lead to the opening of unstable and wider TEMs.

DHA-PL enrichment at the PM leads to a decrease in TEM maximal size and an increase in the number of simultaneous TEMs present in a cell. Strikingly, the total maximum TEM area, obtained as the product of the maximum area per TEM by the number of TEMs, remains constant between OA- and DHA-fed cells. Together with the physical interpretation provided by the cell dewetting model (Boyer et al., 2006; Gonzalez-Rodriguez et al., 2012), this observation suggests a conservation of the global membrane mechanical response at the scale of the entire cell. Essentially, effective membrane tension acting on TEMs behaves as the regulating mechanism. When several TEMs open simultaneously, the relaxation of membrane tension due to the opening of each TEM impacts the other TEMs, because the available membrane material is shared. Thus, for a larger number of simultaneous TEMs, the membrane relaxation felt by each TEM is more pronounced and the TEMs reach a smaller maximum size on average. Therefore, whereas DHA-PL enrichment promotes the frequency of TEM nucleation events by 2-fold, the regulation of membrane mechanical characteristics at the scale of the whole cell appears to be sufficiently robust for the cell to cope with these changes, leading to a conserved total TEM area over the cell. To maintain the overall conservation of the TEM area, DHA-PL-enriched cells compensate for the increase in the nucleation rate by reducing the TEM opening speed and thereby maximal size. Moreover, we record a decrease of lifetime that is ascribed to a reduction in both the phase of latency and closure without affecting the initial opening phase (Fig. S4A,B).

Enrichment of DHA-PLs at the PM decreases the speed of opening, while the time to reach the maximal size is not affected. Consistent with the conserved time frame of TEM opening, we observed that actin organization around TEMs formed in the DHA- and OA-fed cells showed no significant difference. Nevertheless, we observed that TEMs were less stable in the OA-fed cells and were more prone to resume their enlargement. Lower TEM stability may reflect defects in the recruitment or activity of actin-crosslinking proteins around the edge of the TEMs that are yet to be identified. Importantly, we previously reported that the absence of TEM stabilization is linked to massive hemorrhage induced by an ExoC3–chimeric toxin derived from the *B. anthracis* lethal toxin (Rolando et al., 2009). This suggests that DHA might play a key function in the appropriate homeostasis of the endothelial barrier, pointing to a likely role in stabilizing large pore structures that are observed along the vascular system (for a review, see Aird, 2007; Lemichez et al., 2010).

Finally, we found a decrease in cell thickness in the DHA-PL-enriched cells. Applying force to the dorsal part of the PM of normal growing cells is sufficient to bring membranes in close apposition and trigger the nucleation and opening of transcellular pores (Ng et al., 2017). Consistent with this idea, HUVECs intoxicated with ExoC3 were thinner than the control cells, i.e. with medians near the edge of the cells at 332 nm versus 462 nm, respectively (Ng et al., 2017). It is therefore reasonable to think that enriching DHA-PLs may enhance close dorsal and ventral membrane apposition and increase the probability of pore nucleation by reducing the energy cost to initiate a fusion event. As discussed below, changes in the asymmetric distribution of polyunsaturated phospholipids in DHA-PL-enriched cells might contribute to membrane apposition and fusion.

The PM is asymmetric in both lipid classes and lipid unsaturation (Lorent et al., 2020). The outer leaflet contains mostly PC and SM, whereas the inner leaflet contains three major PL classes, namely, PC, PE and PS. Coarse-grained molecular dynamics simulations on

Journal of Cell Science (2022) 135, jcs259119. doi:10.1242/jcs.259119

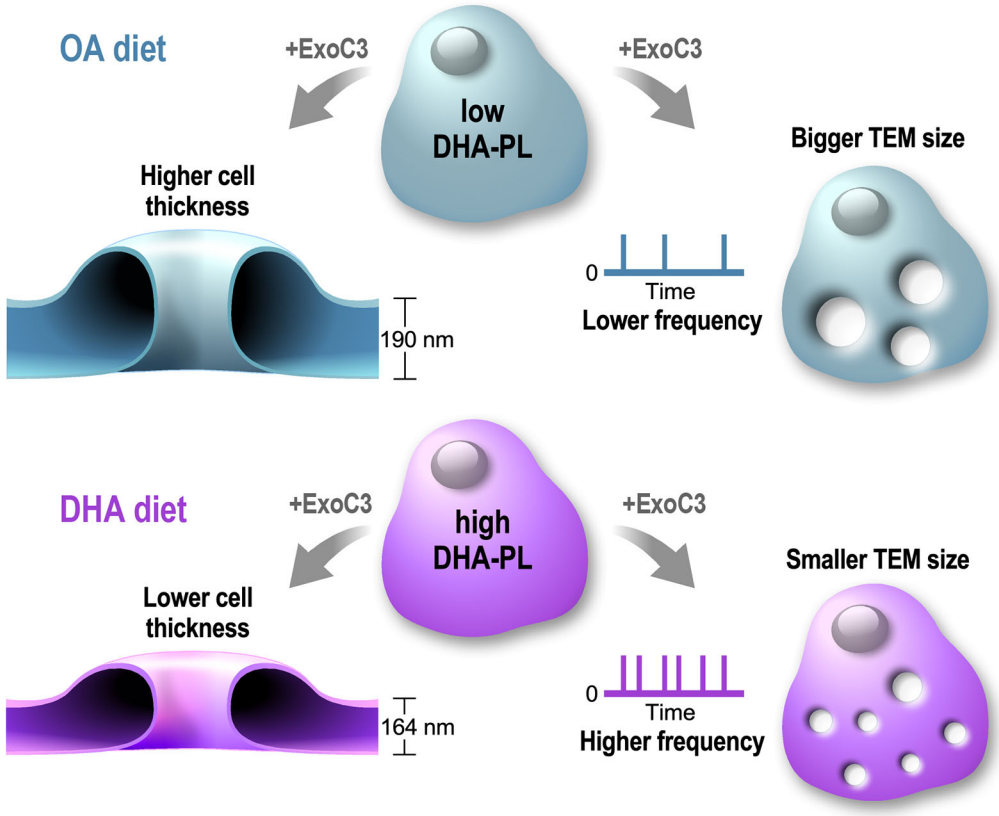

Fig. 7. Impact of polyunsaturated PLs on large-scale membrane deformations induced in endothelial cells challenged with the ExoC3 from *Clostridium botulinum*. The exoenzyme C3 (ExoC3) triggers cycles of nucleation, enlargement and closure of transendothelial cell macroaperture TEM tunnels by inhibiting the small GTPase RhoA and inducing a relaxation of the actomyosin cytoskeleton. The diagram summarizes the cellular effects of a strict diet with either monounsaturated OA (OA diet) or polyunsaturated DHA (DHA diet) on the PM content of DHA-containing phospholipids (DHA-PLs). Comparative analyses show that high levels of DHA-PL increase the frequency of TEM tunnel nucleation, which we link to a decrease in cell thickness, as a reduction in cell height could promote fusion of the basal and dorsal membranes for TEM nucleation. Moreover, we found that the increase in DHA-PLs was also associated with a reduction of the width of TEM tunnels. Together, this shows that endothelial cells self adapt to changes of polyunsaturated phospholipids by maintaining constant the global area of TEM tunnels through modulating their nucleation and cycling kinetics.

asymmetric phospholipid bilayers show that DHA-PLs facilitate membrane tubulation only when they are located on the convex side of the deformation (Tiberti et al., 2020). This effect is due to the ability of DHA-PLs to switch between several twisted conformations in a convex environment, notably to adopt a conformation in which the polyunsaturated acyl chain occupies voids between polar heads and invades the water-lipid interface. DHA-fed cells showed a 10-fold higher content of DHA-PC species at the PM than was evident in the OA-fed cells (16.7% and 1.6%, respectively). In contrast, the amount of DHA-PE and DHA-PS species was only ∼2-fold higher in the DHA-fed HUVECs (18.2% and 14.1%, respectively) than in OA-fed cells (8.8% and 9.5%, respectively). Consequently, the DHA diet might not only increase the overall DHA-PL content of the PM but might also reduce DHA asymmetry because PC is the most affected PL and is quite evenly distributed between the two leaflets. Such a change coupled with the lack of contractile forces mediated by the cytoskeleton, due to the ExoC3 effect, may favor large undulations in the PM. High levels of polyunsaturated PLs on the inner and outer sides of the PM would be beneficial for sustaining large membrane undulations, which are a series of convex and concave deformations. As a prerequisite for hemifusion, the decrease in cell thickness in the DHA-fed cells likely increases the probability of close apposition between the two undulating dorsal and basal membranes, explaining the increase in the frequency and the number of TEMs (Fig. 7). Indeed, as discussed in a review article by Monzel and Sengupta (2016), average membrane undulation amplitudes in nucleated cells have been reported to be of the order of 20–30 nm, and the largest undulations may exceed 100 nm. It is thus reasonable to expect that the largest undulations, whose amplitude are comparable to the cell thickness, facilitate TEM nucleation. Further experimental work on model membrane systems and coarse-grained simulations of TEM formation will help test this idea.

MATERIALS AND METHODS

Reagents

LifeAct-GFP-pCMV plasmid was purchased from Ibidi. Antibodies used in this study were mouse anti-Na^+/K^+ ATPase (cat. no. sc-48345; 1:250; Santa Cruz Biotechnology), annexin II (cat. no. 610068; 1:5000; BD Transduction Laboratories), calregulin (cat. no. sc-373863; 1:500; Santa Cruz Biotechnology), ERGIC53 (cat. no. sc-398777; 1:500; Santa Cruz Biotechnology) and LAMP1 (cat. no. 611042; 1:1000; BD Transduction Laboratories), and sheep anti-TGN46 (cat. no. AHP500G; 1:1000; BioRad). Secondary Alexa Fluor-conjugated antibodies were from Thermo Fisher Scientific and secondary peroxidase-conjugated antibodies were from Jackson ImmunoResearch. For immunofluorescence, Hoechst 33342 and Alexa Fluor-conjugated FITC–phalloidin were purchased from Thermo Fisher Scientific. For STED imaging, Star635–phalloidin was purchased from Abberior. C3 toxin was purified as described previously (Boyer et al., 2006).

Journal of Cell Science (2022) 135, jcs259119. doi:10.1242/jcs.259119

OA and DHA FA (Sigma-Aldrich) were conjugated with FA-free BSA (Sigma-Aldrich). FAs were dissolved in warm (60°C) 200 mM NaOH and conjugated with BSA at the molar ratio of 5:1. The FA-BSA was aliquoted and filled with argon to minimize oxidation. Lipoprotein-depleted serum (LPDS) were prepared as described previously (Renaud et al., 1982). In brief, fetal bovine serum (FBS) was loaded with NaBr to increase density to 1.21 g/ml followed by ultracentrifugation at 220,000 ***g*** at 10°C for 48 h in a Beckman Ti70 rotor. After centrifugation, a greasy layer containing lipoproteins that appeared on the top of the tube was removed and the supernatant was centrifuged again at 220,000 ***g*** at 10°C for 24 h to remove the remaining lipoprotein. Later, the serum was dialyzed intensively with Earle buffer (115 mM NaCl, 5.4 mM KCl, 1.8 mM $CaCl_2$, 0.8 mM $MgSO_4$, 5 mM Hepes, pH 7.4) in a 14 kDa cut-off dialysis membrane (Spectrum) for 72 h and the buffer was refreshed at least five times.

Cell culture, treatment and transfection

HUVECs (PromoCell GmbH, Heidelberg, Germany) were cultured and electroporated, as described in Stefani et al. (2017). In brief, HUVECs were trypsinized and suspended in Ingenio Solution (Mirus) containing plasmid DNA (10 µg per 10^6 cells) in a 4-mm cuvette (CellProjects). Then, cells were electroporated at 300 V, 450 µF, one pulse by GenePulser electroporator (BioRad).

To enrich HUVECs with OA or DHA, cells were washed twice with PBS and lipid starved in LPDS medium [human endothelial SFM (Serum Free Medium; cat. no. 11111-044, Thermo Fisher Scientific), 20% LPDS, 20 ng/ml FGF, 10 ng/ml EGF, 1 µg/ml heparin and Zellshield] overnight with or without 50 µg/ml ExoC3 toxin prepared as described (Boyer et al., 2006). Before experiments, cells were supplemented with 125 µM FA-BSA for 6 h.

Lipid extraction and lipidomics

A modified Bligh and Dyer (1959) extraction was carried out on cell pellets and purified cell membranes in order to extract lipids. Reverse phase liquid chromatography was selected for lipid separation with an UPLC system (Ultimate 3000, Thermo Fisher Scientific). Lipid extracts were separated on an Accucore C18 (150×2.1, 2.5 µm) column (Thermo Fisher Scientific) operated at a 400 µl/min flow rate. The injection volume was 3 µl. Eluent solutions were acetonitrile (ACN)/H_2O at 1:1 (v/v) containing 10 mM ammonium formate and 0.1% formic acid (solvent A), and isopropanol (IPA)/ACN/H_2O 88/10/2 (v/v) containing 2 mM ammonium formate and 0.02% formic acid (solvent B). The step gradient of elution was, in percentage B: 0.0 min, 35%; 0.0–4.0 min, 35% to 60%; 4.0–8.0 min, 60% to 70%; 8.0–16.0 min, 70% to 85%; 16.0–25.0 min, 85 to 97%; 25–25.1 min 97% to 100% B, 25.1–31 min 100% B and finally the column was reconditioned at 35% B for 4 min. The UPLC system was coupled with a Q-exactive plus mass spectrometer (Thermo Fisher Scientific); equipped with a heated electrospray ionization (HESI) probe. This spectrometer was controlled by Xcalibur software (version 4.1.31.9) and operated in electrospray positive mode. Data were acquired with dd-MS2 mode at a resolution of 70,000 for mass spectrometry (MS) and 35,000 for tandem mass spectrometry (MS2) (at 200 *m*/*z*) and a normalized collision energy (NCE) of 25 and 30 eV. Data were reprocessed using LipidSearch 4.1.16 (ThermoFisher). The product search mode was used and the identification was based on the accurate mass of precursor ions and the MS2 spectral pattern. For quantitative comparison of lipid unsaturation, PCs with indistinguishable sn-1 and sn-2 chains were removed from the data. These PC species account for less than 2% of the total PC and have negligeable impact on the analysis.

Fluorescence microscopy

HUVECs were treated as indicated and fixed with 4% paraformaldehyde after 24 h of ExoC3 toxin treatment and after 6 h upon DHA or OA diets corresponding respectively to the maximum of TEM formation and the maximum of DHA incorporation into PLs. Cells were permeabilized with IF buffer (0.05% saponin, 0.2% BSA, phosphate-buffered saline, pH 7.4) and stained with 1:500 dilution of FITC–phalloidin (Thermo Fisher Scientific) for 1 h at room temperature. Images were acquired with Olympus IX83 inverted microscope equipped with a iXon3 camera (Andor) and an UPlanSApo 40×/1.35 NA oil objective (Olympus). The resulting TEM images were analyzed by ImageJ software. The acquired images were segmented by thresholding and the size of cells and TEMs were measured with ImageJ. The number of TEMs per cell was counted manually.

Video microscopy

HUVECs were electroporated with LifeAct-GFP-pCMV as described above and seeded on a gelatin-coated polymer coverslip dish (Ibidi). After recovering for 24 h from transfection, cells were lipid starved in LPDS containing medium overnight. OA-BSA and DHA-BSA were added to the cells to the final concentration of 125 µM for 6 h prior to video recording. Cells were supplemented with 25 mM HEPES (pH 7.4) and recorded on a 37°C heated stage of Nikon Ti inverted microscope using Ultraview spinning disk confocal system (Perkin Elmer). For the TEM opening, images were taken every 10 s for 1 h. For TEM closure, images were taken every 1 min for 3 h to avoid phototoxicity and bleaching during the acquisition. Acquired videos were analyzed with an Icy-based automatic protocol.

Image analysis

Time-lapse videos were analyzed with the Icy software (de Chaumont et al., 2012) and segmentation plugins (http://icy.bioimageanalysis.org/plugin/). Each TEM was first manually identified as a region of interest (ROI). Considering the gradual recruitment of LifeAct–GFP around TEMs, it was difficult to properly identify the edge of TEMs. Indeed, the non-homogeneous contrast at the TEM border leads to a difficult clipping process. To overcome this challenge, we used advanced image analysis methods like the Active Contour plugin to properly track TEM over time. This allowed us in particular to determine the surface of the TEMs at each time point. We then applied a post-processing analysis to filter the TEMs and automatically eliminate remaining wrong segmentations. For instance, we discarded any TEMs that display excessive growing area. In the end, this protocol allowed us to provide precise statistics of the TEM dynamics, such as the evolution of the area, the diameters or the sphericity of TEMs over time.

GPMV preparation

Cells were enriched with OA or DHA as described above followed by induction of blebs as described (Sezgin et al., 2012). Briefly, cells were washed with GPMV buffer (10 mM HEPES, 150 mM NaCl, 2 mM $CaCl_2$, pH 7.4) twice and incubated with GPMV buffer containing 25 mM PFA and 2 mM DTT for 1 h. Blebs were formed and released as GPMVs. Supernatant was collected and centrifuged at 100 ***g*** for 5 min to remove cell debris. For fluorescence microscopy of GPMVs, supernatant containing GPMVs was stained with 5 µg/ml FM 4-64 FX (cat. no. F34653; Thermo Fisher Scientific) in PBS for 30 min. GPMVs were sedimented by gravity on µ-Slide 4-well plates (Ibidi) for 10 min and imaged directly with a Zeiss LSM 780 confocal microscope with a Plan-Apochromat ×63/1.4 oil objective. For western blotting, supernatant containing GPMVs was centrifuged in a Beckman Type 70 Ti rotor at 20,000 ***g*** at 4°C for 1 h. GPMVs appeared as a transparent pellet that was collected for lipidomic analysis or western blotting. Otherwise, cells that did not receive the treatment to induce blebs were collected directly to assess total membranes (TM). For western blotting, TM or GPMV fractions were lysed in clear Laemmli buffer (50 mM Tris-HCl pH 7.4, EDTA 5 mM, 2% SDS) and protein concentration was determined with a BCA assay kit (Thermo Fisher) using BSA suspended in Laemmli buffer as standard. Total membranes or GPMV lysates were adjusted to the same protein quantity between OA and DHA fed cells. Glycerol, β-mercaptoethanol and Bromophenol Blue were added to final concentration of 10%, 5% and 0.004%. Protein samples were analyzed by SDS-PAGE and western blotting. For imaging, cells were plated on a 35 mm µ-Dish (Ibidi), and GPMVs were induced as described above. Cells were then fixed with 4% paraformaldehyde and stained with 1 µg/ml Alexa Fluor 488-WGA (cat. no. W11261; Thermo Fisher Scientific) in PBS for 30 min. After washing with PBS, cells were imaged directly with a Zeiss LSM 780 confocal microscope with a Plan-Apochromat ×63/1.4 oil objective.

STED microscopy

Cells were grown on H1.5 glass coverslips coated with 10 µg/ml fibronectin. After treatment, cells were fixed with 4% PFA with 0.1% glutaraldehyde for 15 min at room temperature. Cells were washed with PBS, quenched in 50 mM NH_4Cl for 15 min followed by permeabilizing in IF buffer (PBS, 0.05% saponin and 0.2% BSA) for 30 min. Afterwards, the cells were stained with 1 µM Star635–phalloidin (Abberior) for 1 h followed by three washes with IF buffer for 5 min and a final wash in H_2O. The cells were mounted in Mount Solid Antifade (Abberior) following manufacturer's instruction. Stimulated emission depletion (STED) imaging was performed by TCS STED SP8 (Leica) using a APO 93×/1.3 NA motCORR lens. The excitation laser was at 633 nm and pulse depletion laser at 775 nm. STED images were deconvolved using Huygens with five iterations.

Atomic force microscope measurement of TEM topology

AFM experiments were carried out on a JPK NanoWizardIII mounted on a Zeiss Axio Observer.Z1. For the elasticity measurements, PFQNM-LC-A-Cal cantilevers (Bruker) with a 140 nm diameter spherical tip apex were used and calibrated using the SNAP calibration method (Schillers et al., 2017). The AFM was operated in QI mode on the perinuclear region of living cells to record a 10 µm^2, 20×20 pixels map of force curves with 2 µm ramp length, 200 pN force trigger and 50 µm/s tip velocity. Force maps were computed using in-house software (pyAF; Janel et al., 2019) for the fitting of the indentation up to 40 nm using the Hertz model. Each dot of the scatter plot corresponds to a different cell (median of a map). For the topography measurements of TEMs, sharper Olympus AC40 cantilevers were used with the SADER calibration method (Sader et al., 2016). Cells had to be fixed with 4% PFA in PBS for 10 min because of the short window of time available for the measurement with the microscope. A QI map of 150×150 pixels bigger than the size of the TEM was recorded with an 800 nm ramp and 100 µm/s tip velocity. We then computed the zero-force topography by determining the point of contact, and drew several profiles across the TEM to measure its diameter and the height of the rim and the cell at the border. This was all performed on the JPK analysis software v6. Each dot of the scatter plot corresponds to a TEM.

RhoA ADP-ribosylation assay

HUVECs were seeded in 15 cm culture plates and treated with or without 50 µg/ml ExoC3 toxin in LPDS or FBS medium (human endothelial SFM, 20% serum, 20 ng/ml FGF, 10 ng/ml EGF, 1 µg/ml heparin and Zellshield) overnight. Before experiments, cells were supplemented with 125 µM FA-BSA for 6 h. Cells were lysed in ADP-ribosylation buffer (20 mM Tris-HCl, 1 mM EDTA, 1 mM DTT, 5 mM $MgCl_2$ and cOmpleteTM, pH 7.5) by passing through a 27G syringe 20 times. Cell lysates were collected by centrifugation at 12,000 ***g*** for 10 min and the protein concentration was determined by BCA assay (Thermo Fisher Scientific). Reaction was carried out by incubating 20 µg of cell lysate with 2 µg ExoC3 and 10 µM 6-biotin-17-NAD$^+$ (BioLog) at 37°C 30 min. The reaction was terminated by addition of 1 mM DTT and Laemmli buffer (0.3 M Tris-HCl, 10% SDS, 37.5% glycerol and 0.4 mM Bromophenol Blue) and boiled at 100°C for 5 min. The samples were subjected to 12% SDS-PAGE and ADP-ribosylated (i.e. biotin-labeled) RhoA was detected by western blotting using streptavidin–peroxidase.

Physical model of TEM opening

In the physical model for TEM opening dynamics (Gonzalez-Rodriguez et al., 2012), the driving force for opening is given by:

$$F_d = 2\sigma - \frac{\tilde{T}}{R},$$

where σ is the membrane tension, $\tilde{T}$ is the line tension and R is the TEM radius. The membrane tension σ depends on R through Helfrich's law, which here we write in a generalized form to account for the coexistence of N simultaneous TEMs in the same cell:

$$\sigma = \sigma_0 \exp\left[-\frac{\left(\sum_{i=1}^{N} R_i\right)^2}{NR_c^2}\right],$$

where $R_c^2 = (R_{cell}^2 k_B T)/(8\pi\kappa)$ is the so-called critical radius, with R_{cell} the total cell radius, k_B the Boltzmann constant, T the temperature, and κ the effective membrane bending rigidity. Owing to actin cable polymerization around the TEM, the line tension is not a constant but rather it increases with time (Stefani et al., 2017), which can be represented by a linear increase $\tilde{T} \sim \alpha t$. The dynamics of TEM opening are governed by a balance between driving force and cell-substrate friction, characterized by a friction coefficient µ. For the case of N identical TEMs, this balance results in the following differential equation:

$$\mu R^2 \frac{dR}{dt} = 2\sigma_0 R \exp\left(-\frac{NR^2}{R_c^2}\right) - \alpha t.$$

This equation can be solved numerically. However, insight can be gained by analytical approximations. First, in the asymptotic short-time limit (limit $t \to 0$), when R is small, the equation can be approximated as

$$v_i = \frac{dA}{dt} = \frac{4\pi\sigma_0}{\mu},$$

where $A=\pi R^2$ is the TEM area. Therefore, the initial TEM opening speed, v_i, is proportional to the undisturbed cell membrane tension σ_0.

Second, the dependence of the maximum TEM area $A_{max} = \pi R_{max}^2$ on the membrane parameters σ_0 and κ can be estimated by the following approximation. Let us suppose that the initial opening speed v_i is an acceptable estimate of the average opening speed. Then, the opening time t_{max} is related to the maximum TEM area by

$$t_{max} \approx \frac{\mu A_{max}}{4\pi\sigma_0}.$$

Moreover, at $t=t_{max}$, the opening stops and $dR/dt=0$. By replacing these two results in the differential equation, we obtain the following approximate relationship:

$$x \exp x^2 = \frac{8\sqrt{N}\sigma_0^2}{\mu\alpha R_c},$$

where we have defined $x = \sqrt{N}R_{max}/R_c$. The nondimensional parameter on the right-hand side of this expression is slightly larger than 1, which requires x to be of the order of or somewhat larger than 1. In this range of values, small changes in x yield large changes of the exponential function, implying that x is weakly dependent on the right-hand side. Therefore, x will remain approximately constant for moderate changes of σ_0, implying that $N^{1/2}R_{max} \sim R_c \sim 1/\kappa^{1/2}$. This result shows that the maximum TEM size is very sensitive to κ but rather insensitive to σ_0. We thus obtain the following estimate of the effective membrane bending rigidity:

$$\kappa \approx \frac{k_B T A_{cell}}{8\pi N A_{max}}.$$

Statistical analysis

Data are shown as the mean±s.e.m. or median±c.i. or range when indicated. The normality distribution of the data was first calculated using Kolmogorov–Smirnov test. For Gaussian distributed data, an unpaired two-tailed Student's *t*-test was used for comparing two groups and one-way ANOVA with Bonferroni post-hoc corrections was used for multiple group comparison. For non-Gaussian distributed data, unpaired, two-tailed Mann–Whitney test was used. *P*-values are indicated *P<0.05, **P<0.01, ***P<0.001 and ****P<0.0001 and considered statistically significant. The statistical software used was Prism 8 (GraphPad Software, San Diego, CA, USA).

Acknowledgements
We thank Blandine Madji Hounoum for pilot lipidomics experiments, Frédéric Brau and Sophie Abelanet for support in light and STED microscopy, James Muncey for help in time-lapse analyses with Icy software, Marco Lorenzi (INRIA, Sophia Antipolis) for comments on the manuscript and all members of our laboratories for discussion.

Competing interests
The authors declare no competing or financial interests.

Author contributions
Conceptualization: E.L., H.B.; Methodology: L.F., S.J., D.G.-R., D.D., F.L., E.L., H.B.; Software: S.D., J.-C.O.-M.; Validation: M.-C.T., L.F., S.J., D.G.-R., D.D., F.L., E.L., H.B.; Formal analysis: M.-C.T., L.F., S.J., D.G.-R., E.L., H.B.; Investigation: M.-C.T., L.F., S.J., D.G.-R., E.L., H.B.; Resources: C.M., A.M., D.D., E.L., H.B.; Data curation: M.-C.T., L.F., S.J., E.L., H.B.; Writing - original draft: M.-C.T., D.G.-R., E.L., H.B.; Writing - review & editing: M.-C.T., S.J., D.G.-R., B.A., E.L., H.B.; Visualization: M.-C.T., S.J., D.G.-R., E.L., H.B.; Supervision: E.L., H.B.; Project administration: E.L., H.B.; Funding acquisition: J.-C.O.-M., B.A., F.L., E.L., H.B.

Funding
This work was supported by a grant from the Fondation pour la Recherche Médicale (Convention DEQ20180339156 Equipes FRM 2018), the Agence Nationale de la Recherche (ANR-11-LABX-0028-01, ANR-15-CE18-0016, ANR 10-EQPX-04-01, ANR-10-INBS-04 and ANR-10-LABX-62-IBEID) and FEDER 12001407, and partially by grants from the France-BioImaging infrastructure (ANR-10-INBS-04) and the Labex IBEID (ANR-10-LABX-62-IBEID). M.-C.T. was supported by a PhD fellowship from the Labex Signalife PhD Programme and by the Fondation pour la Recherche Médicale (Contrat FDT201904008135).

Peer review history
The peer review history is available online at https://journals.biologists.com/jcs/article-lookup/doi/10.1242/jcs.259119.

References

Aird, W. C. (2007). Vascular bed-specific thrombosis. *J. Thromb. Haemost.* **5**, 283-291. doi:10.1111/j.1538-7836.2007.02515.x

Antonny, B., Vanni, S., Shindou, H. and Ferreira, T. (2015). From zero to six double bonds: phospholipid unsaturation and organelle function. *Trends Cell Biol.* **25**, 427-436. doi:10.1016/j.tcb.2015.03.004

Barelli, H. and Antonny, B. (2016). Lipid unsaturation and organelle dynamics. *Curr. Opin. Cell Biol.* **41**, 25-32. doi:10.1016/j.ceb.2016.03.012

Bazinet, R. P. and Layé, S. (2014). Polyunsaturated fatty acids and their metabolites in brain function and disease. *Nat. Rev. Neurosci.* **15**, 771-785. doi:10.1038/nrn3820

Bligh, E. G. and Dyer, W. J. (1959). A rapid method of total lipid extraction and purification. *Can. J. Biochem. Physiol.* **37**, 911-917. doi:10.1139/y59-099

Boyer, L., Doye, A., Rolando, M., Flatau, G., Munro, P., Gounon, P., Clément, R., Pulcini, C., Popoff, M. R., Mettouchi, A. et al. (2006). Induction of transient macroapertures in endothelial cells through Rho inhibition by *Staphylococcus aureus* factors. *J. Cell Biol.* **173**, 809-819. doi:10.1083/jcb.200509009

Braakman, S. T., Pedrigi, R. M., Read, A. T., Smith, J. A. E., Stamer, W. D., Ethier, C. R. and Overby, D. R. (2014). Biomechanical strain as a trigger for pore formation in Schlemm's canal endothelial cells. *Exp. Eye Res.* **127**, 224-235. doi:10.1016/j.exer.2014.08.003

Braakman, S. T., Moore, J. E., Ethier, C. R. and Overby, D. R. (2016). Transport across schlemm's canal endothelium and the blood-aqueous barrier. *Exp. Eye Res.* **146**, 17-21. doi:10.1016/j.exer.2015.11.026

Caires, R., Sierra-Valdez, F. J., Millet, J. R. M., Herwig, J. D., Roan, E., Vásquez, V. and Cordero-Morales, J. F. (2017). Omega-3 fatty acids modulate trpv4 function through plasma membrane remodeling. *Cell Rep.* **21**, 246-258. doi:10.1016/j.celrep.2017.09.029

de Chaumont, F., Dallongeville, S., Chenouard, N., Hervé, N., Pop, S., Provoost, T., Meas-Yedid, V., Pankajakshan, P., Lecomte, T., Le Montagner, Y. et al. (2012). Icy: An open bioimage informatics platform for extended reproducible research. *Nat. Methods* **9**, 690-696. doi:10.1038/nmeth.2075

Gonzalez-Rodriguez, D., Maddugoda, M. P., Stefani, C., Janel, S., Lafont, F., Cuvelier, D., Lemichez, E. and Brochard-Wyart, F. (2012). Cellular dewetting: opening of macroapertures in endothelial cells. *Phys. Rev. Lett.* **108**, 218105. doi:10.1103/PhysRevLett.108.218105

Harayama, T. and Riezman, H. (2018). Understanding the diversity of membrane lipid composition. *Nat. Rev. Mol. Cell Biol.* **19**, 281-296. doi:10.1038/nrm.2017.138

Helfrich, W. (1973). Elastic properties of lipid bilayers: Theory and possible experiments. *Z. Nat. Teil C: Biochem. Biophys. Biol. Virol.* **28**, 693-703. doi:10.1515/znc-1973-11-1209

Iizuka-Hishikawa, Y., Hishikawa, D., Sasaki, J., Takubo, K., Goto, M., Nagata, K., Nakanishi, H., Shindou, H., Okamura, T., Ito, C. et al. (2017). Lysophosphatidic acid acyltransferase 3 tunes the membrane status of germ cells by incorporating docosahexaenoic acid during spermatogenesis. *J. Biol. Chem.* **292**, 12065-12076. doi:10.1074/jbc.M117.791277

Janel, S., Popoff, M., Barois, N., Werkmeister, E., Divoux, S., Perez, F. and Lafont, F. (2019). Stiffness tomography of eukaryotic intracellular compartments by atomic force microscopy. *Nanoscale* **11**, 10320-10328. doi:10.1039/c8nr08955h

Jeffrey, B. G. and Neuringer, M. (2009). Age-related decline in rod phototransduction sensitivity in rhesus monkeys fed an n-3 fatty acid–deficient diet. *Invest. Ophthalmol. Vis. Sci.* **50**, 4360-4367. doi:10.1167/iovs.09-3640

Lemichez, E., Lecuit, M., Nassif, X. and Bourdoulous, S. (2010). Breaking the wall: targeting of the endothelium by pathogenic bacteria. *Nat. Rev. Micro.* **8**, 93-104. doi:10.1038/nrmicro2269

Lemichez, E., Gonzalez-Rodriguez, D., Bassereau, P. and Brochard-Wyart, F. (2013). Transcellular tunnel dynamics: control of cellular dewetting by actomyosin contractility and I-bar proteins. *Biol. Cell* **105**, 109-117. doi:10.1111/boc.201200063

Levayer, R. and Lecuit, T. (2012). Biomechanical regulation of contractility: Spatial control and dynamics. *Trends Cell Biol.* **22**, 61-81. doi:10.1016/j.tcb.2011.10.001

Levental, K. R., Malmberg, E., Symons, J. L., Fan, Y.-Y., Chapkin, R. S., Ernst, R. and Levental, I. (2020). Lipidomic and biophysical homeostasis of mammalian membranes counteracts dietary lipid perturbations to maintain cellular fitness. *Nat. Commun.* **11**, 1339. doi:10.1038/s41467-020-15203-1

Lorent, J. H., Levental, K. R., Ganesan, L., Rivera-Longsworth, G., Sezgin, E., Doktorova, M., Lyman, E. and Levental, I. (2020). Plasma membranes are asymmetric in lipid unsaturation, packing and protein shape. *Nat. Chem. Biol.* **16**, 644-652. doi:10.1038/s41589-020-0529-6

Maddugoda, M. P., Stefani, C., Gonzalez-Rodriguez, D., Saarikangas, J., Torrino, S., Janel, S., Munro, P., Doye, A., Prodon, F., Aurrand-Lions, M. et al. (2011). cAMP signaling by anthrax edema toxin induces transendothelial cell tunnels, which are resealed by MIM via Arp2/3-driven actin polymerization. *Cell Host Microbe* **10**, 464-474. doi:10.1016/j.chom.2011.09.014

Manni, M. M., Tiberti, M. L., Pagnotta, S., Barelli, H., Gautier, R. and Antonny, B. (2018). Acyl chain asymmetry and polyunsaturation of brain phospholipids facilitate membrane vesiculation without leakage. *eLife* **7**, e34394. doi:10.7554/eLife.34394

Monzel, C. and Sengupta, K. (2016). Measuring shape fluctuations in biological membranes. *J. Phys. D Appl. Phys.* **49**, 243002. doi:10.1088/0022-3727/49/24/243002

Munro, P., Benchetrit, M., Nahori, M.-A., Stefani, C., Clément, R., Michiels, J.-F., Landraud, L., Dussurget, O. and Lemichez, E. (2010). The *Staphylococcus aureus* epidermal cell differentiation inhibitor toxin promotes formation of infection foci in a mouse model of bacteremia. *Infect. Immun.* **78**, 3404-3411. doi:10.1128/IAI.00319-10

Ng, W. P., Webster, K. D., Stefani, C., Schmid, E. M., Lemichez, E., Bassereau, P. and Fletcher, D. A. (2017). Force-induced transcellular tunnel formation in endothelial cells. *Mol. Biol. Cell* **28**, 2650-2660. doi:10.1091/mbc.e17-01-0080

Pinot, M., Vanni, S., Pagnotta, S., Lacas-Gervais, S., Payet, L.-A., Ferreira, T., Gautier, R., Goud, B., Antonny, B. and Barelli, H. (2014). Polyunsaturated phospholipids facilitate membrane deformation and fission by endocytic proteins. *Science* **345**, 693-697. doi:10.1126/science.1255288

Randall, A. S., Liu, C.-H., Chu, B., Zhang, Q., Dongre, S. A., Juusola, M., Franze, K., Wakelam, M. J. O. and Hardie, R. C. (2015). Speed and sensitivity of phototransduction in drosophila depend on degree of saturation of membrane phospholipids. *J. Neurosci.* **35**, 2731-2746. doi:10.1523/JNEUROSCI.1150-14.2015

Renaud, J.-F., Scanu, A. M., Kazazoglou, T., Lombet, A., Romey, G. and Lazdunski, M. (1982). Normal serum and lipoprotein-deficient serum give different expressions of excitability, corresponding to different stages of differentiation, in chicken cardiac cells in culture. *Proc. Natl. Acad. Sci. USA* **79**, 7768-7772. doi:10.1073/pnas.79.24.7768

Rolando, M., Munro, P., Stefani, C., Auberger, P., Flatau, G. and Lemichez, E. (2009). Injection of *Staphylococcus aureus* EDIN by the *Bacillus anthracis* protective antigen machinery induces vascular permeability. *Infect. Immun.* **77**, 3596-3601. doi:10.1128/IAI.00186-09

Romero, L. O., Massey, A. E., Mata-Daboin, A. D., Sierra-Valdez, F. J., Chauhan, S. C., Cordero-Morales, J. F. and Vásquez, V. (2019). Dietary fatty acids fine-tune piezo1 mechanical response. *Nat. Commun.* **10**, 1200. doi:10.1038/s41467-019-09055-7

Sader, J. E., Borgani, R., Gibson, C. T., Haviland, D. B., Higgins, M. J., Kilpatrick, J. I., Lu, J., Mulvaney, P., Shearer, C. J., Slattery, A. D. et al. (2016). A virtual instrument to standardise the calibration of atomic force microscope cantilevers. *Rev. Sci. Instrum.* **87**, 093711. doi:10.1063/1.4962866

Salbreux, G., Charras, G. and Paluch, E. (2012). Actin cortex mechanics and cellular morphogenesis. *Trends Cell Biol.* **22**, 536-545. doi:10.1016/j.tcb.2012.07.001

Schillers, H., Rianna, C., Schäpe, J., Luque, T., Doschke, H., Wälte, M., Uriarte, J. J., Campillo, N., Michanetzis, G. P. A., Bobrowska, J. et al. (2017).

Standardized nanomechanical atomic force microscopy procedure (snap) for measuring soft and biological samples. *Sci. Rep.* **7**, 5117. doi:10.1038/s41598-017-05383-0

Schimmel, L., Heemskerk, N. and van Buul, J. D. (2017). Leukocyte transendothelial migration: a local affair. *Small GTPases* **8**, 1-15. doi:10.1080/21541248.2016.1197872

Sezgin, E., Kaiser, H.-J., Baumgart, T., Schwille, P., Simons, K. and Levental, I. (2012). Elucidating membrane structure and protein behavior using giant plasma membrane vesicles. *Nat. Protoc.* **7**, 1042-1051. doi:10.1038/nprot.2012.059

Shindou, H., Koso, H., Sasaki, J., Nakanishi, H., Sagara, H., Nakagawa, K. M., Takahashi, Y., Hishikawa, D., Iizuka-Hishikawa, Y., Tokumasu, F. et al. (2017). Docosahexaenoic acid preserves visual function by maintaining correct disc morphology in retinal photoreceptor cells. *J. Biol. Chem.* **292**, 12054-12064. doi:10.1074/jbc.M117.790568

Stefani, C., Gonzalez-Rodriguez, D., Senju, Y., Doye, A., Efimova, N., Janel, S., Lipuma, J., Tsai, M. C., Hamaoui, D., Maddugoda, M. P. et al. (2017). Ezrin enhances line tension along transcellular tunnel edges via NMIIa driven actomyosin cable formation. *Nat. Commun.* **8**, 15839. doi:10.1038/ncomms15839

Tanguy, E., Costé de Bagneaux, P., Kassas, N., Ammar, M.-R., Wang, Q., Haeberlé, A.-M., Raherindratsara, J., Fouillen, L., Renard, P.-Y., Montero-Hadjadje, M. et al. (2020). Mono- and poly-unsaturated phosphatidic acid regulate distinct steps of regulated exocytosis in neuroendocrine cells. *Cell Rep.* **32**, 108026. doi:10.1016/j.celrep.2020.108026

Tiberti, M. L., Antonny, B. and Gautier, R. (2020). The transbilayer distribution of polyunsaturated phospholipids determines their facilitating effect on membrane deformation. *Soft Mat.* **16**, 1722-1730. doi:10.1039/C9SM02107H

Tixier-Vidal, A., Picart, R., Loudes, C. and Bauman, A. F. (1986). Effects of polyunsaturated fatty acids and hormones on synaptogenesis in serum-free medium cultures of mouse fetal hypothalamic cells. *Neuroscience* **17**, 115-132. doi:10.1016/0306-4522(86)90230-7

van Meer, G., Voelker, D. R. and Feigenson, G. W. (2008). Membrane lipids: Where they are and how they behave. *Nat. Rev. Mol. Cell Biol.* **9**, 112-124. doi:10.1038/nrm2330

Yuki, K., Shindou, H., Hishikawa, D. and Shimizu, T. (2009). Characterization of mouse lysophosphatidic acid acyltransferase 3: an enzyme with dual functions in the testis. *J. Lipid Res.* **50**, 860-869. doi:10.1194/jlr.M800468-JLR200